nature physics

SUPPLEMENTARY INFORMATION

DOI: 10.1038/NPHYS3013

Demonstration of magnetically activated and guided isotope separation

We present in this supplement technical details for the source, optical pumping scheme, magnet array, and detection apparatus used in this experiment. We then explain the generality of the magnetic separation, particularly discussing its mass independence. We additionally provide a table (Supplementary Table 1) of 129 candidate isotopes for our method. For each of these isotopes, we identify a target state and relevant wavelengths for optical pumping. Supplementary Table 1 includes supplementary references providing spectroscopic information for those isotopes considered.

Apparatus Details

Source

Three generations of sources were used for this work. The first source was a stainless steel reservoir (with approximately 20 cm^3 volume) that could be resistively heated to up to 625 ºC. Evaporated lithium exited the reservoir through a 1 cm diameter tube. We loaded this source with several grams of enriched Li-6 for investigating Li-6 depletion using the RGA. The subsequent two sources, also stainless steel reservoirs, included larger volumes for loading tens of grams of material at a time (75 and 200 cm^3, respectively) and allowed for continuous operation at higher temperatures (up to 750 ºC). Lithium likewise exited these sources through a 1 cm tube, but this tube was heated to a temperature of 50 ºC beyond the reservoir temperature to prevent clogging due to condensation after prolonged use at high temperature. We used these sources for measuring Li-6 suppression via fluorescence when using natural lithium, and also for characterizing throughput and efficiency. For all measurements, we used feedback (proportional-integral-derivative) controllers for stabilizing the source temperature (as indicated

DOI: 10.1038/NPHYS3013

via type-K thermocouples) to within ±1 ºC. A 1 mm wide by 10 mm high slit is located close to 10 cm beyond the output of the reservoir (with the exact distance depending on the source used). A narrow slit was chosen to provide a well-defined initial location for the atom trajectories. For the second and third generation sources this slit was heated to beyond the source operating temperature to ensure that the slit did not become obstructed after prolonged evaporation of material from the source.

Optical pumping

Optical pumping is performed along one arm of a 6-way cross perpendicular to the atomic beam axis. Another arm is used to image fluorescence onto a CCD camera. The optical pumping light is provided by a tapered amplifier seeded by a grating-stabilized external cavity diode laser (ECDL). This arrangement ultimately provides close to 150 mW of 671 nm light through a fiber for the optical pumping. The frequency of this laser is stabilized to the Li-6 D1 line via an offset lock [27] that is referenced to another ECDL whose frequency is stabilized via saturated absorption spectroscopy. The initial laser bandwidth (<6 MHz) can be broadened to as much as 50 MHz by double-passing the light through an electro-optic modulator driven at a frequency of 6 MHz [28].

The beam is then expanded to an elliptical shape that is approximately 4 cm wide by 2 cm high and passed through the cross. Typical peak intensities reach >30 mW cm^{-2}. While the laser yields up to 150 mW of usable power, Li-6 suppression is insensitive to substantially reducing the laser power. Supplementary Fig. 1 shows sample measurements of Li-6 suppression over a range of laser powers. Supplementary Fig. 1(A) gives suppression (measured using RGA) when operating our source at 600 ºC using enriched Li-6. Supplementary Fig. 1(B) shows depletion (measured via fluorescence) when operating our source at 650 ºC using natural lithium. The laser powers shown in Supplementary Fig. 1(A) were measured by focusing the light that passes

through the optical pumping region onto a laser power meter. In contrast, laser powers for Supplementary Fig. 1(B) were measured before the beam shaping optics. To thus avoid direct comparison, we give powers in Supplementary Fig. 1(B) as fractional powers. The peak intensity at the highest laser power in Supplementary Fig. 1(A) (35 mW) is roughly 13 mW cm^{-2}. Note that for these data we used the thickness monitor to measure the flux in the pumping region corresponding to the given temperatures. Future work will examine the laser intensity dependence of the depletion in more detail.

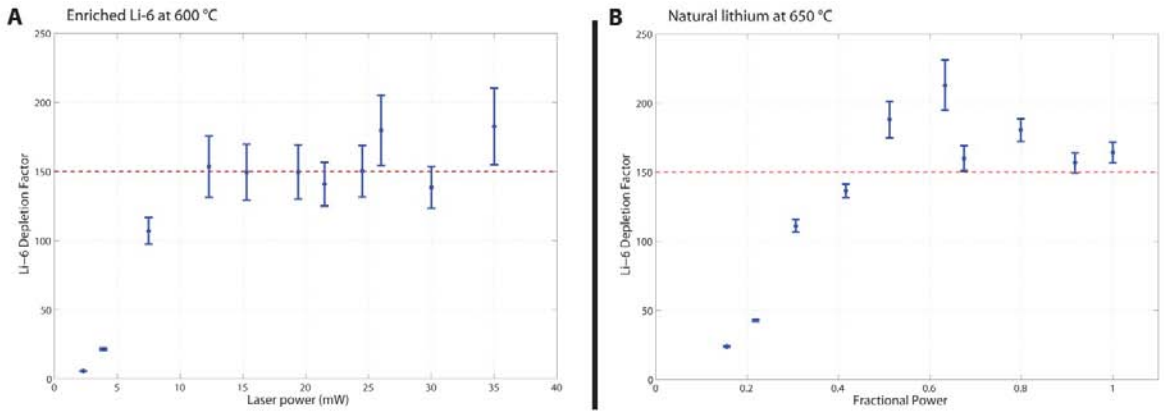

Supplementary Figure 1: Comparison of Li-6 suppression over a range of laser powers. (A) Measurements using enriched Li-6 while operating the source at 600 ºC. (B) Measurements using natural lithium while operating the source at 650 ºC. Using the thickness monitor, we measure the deposition rates in the pumping region for these two data sets to be 0.503 ± 0.004 Å/s and 0.341 ± 0.001 Å/s respectively. Note that different sources were used for these data sets. Error bars show standard deviations from the mean.

The laser frequency is adjusted to drive Li-6 atoms from the $^2S_{1/2}$ (F=3/2) ground state to the $^2P_{1/2}$ (F'=3/2) excited state. After scattering a few photons, Li-6 atoms decay into the $^2S_{1/2}$ (F=1/2) ground state. In external magnetic fields over 30 gauss, atoms in the F = 1/2 ground state are entirely high-field seeking, decreasing in energy in increasing magnetic field [22], and will thus be attracted to the magnets. The 228 MHz splitting between the F = 1/2 and F = 3/2 ground states is sufficient to prevent the laser from pumping Li-6 atoms directly out of the F = 1/2 state. Systematic effects that may contaminate the Li-6 polarization include inelastic collisions,

DOI: 10.1038/NPHYS3013

radiation trapping, Majorana spin-flips, and stray light. The first two effects can be attenuated by reducing the atomic density in the optical pumping region. This can be achieved without sacrificing throughput by increasing the distance between the source and optical pumping region and broadening the laser beam size. To maximize the optical pumping rate, the laser should be above saturation intensity. We suspect that our depletion might be limited due to not reaching saturation intensity over a sufficiently large area (for maximizing the interaction time while at or above saturation intensity).

Magnet array

The source and optical pumping cross are connected via a 63 mm diameter bellows to a 1.93 m x 0.28 m x 0.20 m aluminum chamber with Viton o-ring seals. A large 550 l s^{-1} turbopump keeps the pressure below 1 x 10^{-7} Torr. The 1.5 m long array of NdFeB magnets consists of 15 panels of 32 magnets and is curved over its length by just 20 mrad. Each magnet is 38 mm long x 3.175 mm wide x 3.175 mm thick with its magnetization directed through its thickness. The magnets in each panel are arranged in a Halbach configuration where the magnetization vector is rotated by 90 degrees about the magnet length between adjacent magnets. This arrangement essentially cancels the magnetic field on one face of a panel but amplifies the field on the opposite face to close to 1 T in proximity to the magnets. A 0.05 mm stainless steel shim conforms to the surface of the array to prevent lithium from contaminating the magnets. Fig. 3(C) shows discrepancy between the shape of the throughput predicted by numerical simulation and the actual throughput measured by a wire trace. We attribute these differences to the exact shape of the magnet array: the array consists of discrete panels and the miniscule angles between panels likely do not perfectly match the simulated angles.

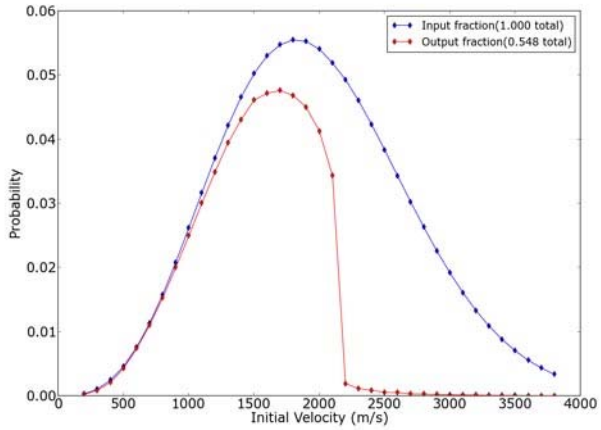

Supplementary Figure 2: Sample numerical simulation. The blue trace shows a thermal velocity distribution from a Li source at 800 K. The red trace shows the distribution of the remaining atoms after the guide produced by a numerical simulation, assuming all of the atoms entered the magnetic guide in the low-field seeking ground state ($m_j = +1/2$ in sufficiently large magnetic fields). The simulation was done using Li-6 as the source material but Li-7 behavior is very similar.

Numerical simulation suggests that atoms beyond a certain cut-off velocity cannot be deflected by the magnet array. This cut-off velocity corresponds to when the velocity component perpendicular to the face of the magnets becomes larger than the maximum magnetic potential determined by the Halbach array. Supplementary Fig. 2 displays this concept in a simulated velocity distribution at the output of the magnets compared to the initial 800 K thermal velocity distribution leaving the source. As the incidence angle on the magnets increases the cut-off velocity moves to lower values, reducing the efficiency. Supplementary Fig. 2, which was generated with the source at its optimal location just avoiding line-of-sight, indicates 55% efficiency for low-field seeking atoms.

Detection and measurements

Relative abundances

The RGA consists of an ionization source (sampling the collection plane) followed by a quadrupole mass filter and electron multiplier. The dynamic range of the RGA is large enough to measure suppression of enriched Li-6 by more than 99% when operating the source at 550 ºC and beyond. The RGA also allows us to confirm that Li-7 throughput is not effected by the

DOI: 10.1038/NPHYS3013

optical pumping. We positioned the RGA close to where the throughput is maximal, however the RGA cannot translate. When using natural lithium, the signal at mass 7 amu "bleeds" into the mass 6 amu signal, making determination of Li-6 suppression difficult.

To measure fluorescence, we position a 3" diameter lens as close as possible (about 15 cm) to the fluorescence beyond the magnets. We choose the focal length to achieve close to one-to-one imaging of the fluorescence onto the cooled CCD sensor. Exposure times for fluorescence measurements are typically several seconds. Prior to passing through the chamber, the fluorescence beam double-passes an acousto-optic modulator in order to generate an additional beam 228 MHz detuned from the optical pumping beam. The resulting beams then pump Li-6 atoms out of both the F = 1/2 and F = 3/2 ground states, maximizing fluorescence.

For both RGA and fluorescence measurements we make three sets of measurements for obtaining a depletion factor. These include signals with and without optical pumping, and also a signal with the atomic beam blocked just beyond the source exit. We extract depletion factors as the ratio of background subtracted signals without and with optical pumping. While we use a narrow-band filter to reduce the effect of stray light on the fluorescence measurements, scattered light at 670 nm contributes to a background that limits signal-to-noise. The background on the RGA at masses 6 and 7, shown in the grey trace in Fig. 3, likely comes from lithium deposition near the ionization region of the RGA. This background can build up over time, ultimately leading to worsening signal-to-noise. We make measurements over short durations during which the background does not appreciably change. We periodically degas the RGA by locally heating the ionization region to mitigate lithium contamination.

Throughput and efficiency

The wire detector supplements the RGA and fluorescence measurements by providing the lateral profile of the throughput, confirming drastic suppression of Li-6 over the entire collection plane. The wire detector also provides a measure of total flux, but we lack an accurate calibration for both its ionization and detection efficiency. The detection efficiency is particularly sensitive to the rhenium temperature, which is determined by the voltage across the ribbon. We use the thickness monitor, whose sensor is 8.25 mm in diameter, to calibrate the wire detector. Thickness monitor measurements beyond the magnets correspond to the convolution of the actual throughput over the sensor area with the response function of the thickness monitor. To measure the response function, we translated the thickness monitor across a 1 mm wide slit in the optical pumping region where the flux is uniform. These measurements give the convolution of the actual response function with a 1 mm wide step function. We therefore approximate the response function as a Gaussian, as shown in Supplementary Fig. 3, whose convolution with the 1 mm wide step function returns the measurements made in the pumping region [29].

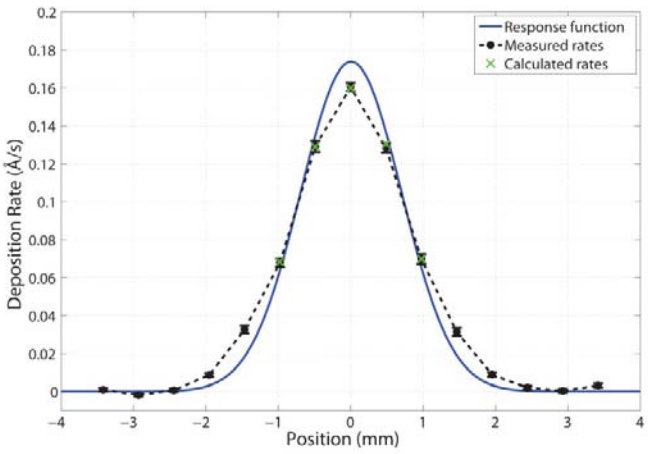

Supplementary Figure 3: Response function measurement. The black data points show deposition rates obtained by translating the thickness monitor across a 1 mm wide slit in the optical pumping region. With these measurements, we obtain a Gaussian curve (blue trace) whose convolution with a 1 mm step function at the position corresponding to any data point (green crosses) reasonably reproduces that data point. Error bars show standard deviations from the mean.

We approximate the actual spatial profile of the throughput beyond the magnets by the wire detector traces. In fact, these traces correspond to a convolution of the actual throughput with an

DOI: 10.1038/NPHYS3013

800 μm wide step function. We choose a scaling factor for the wire detector trace such that the convolutions of the scan with the response function at specified points reasonably recreate the thickness monitor measurements. With a suitable scaling factor, we can finally estimate the throughput by integrating the scaled wire detector trace across the entire collection plane. We derive the uncertainty for the scaling factor from the maximal deviation of the calculated deposition rates (obtained from the convolution described above) to the measured rates. To estimate the efficiency of the guide, we first measure the flux in the pumping region as a function of source temperature using the thickness monitor, and use this flux to infer the throughput at the 15 mm wide aperture at the entrance of the magnet array. We then compare this flux to the measured throughput beyond the magnets.

Applicability of MAGIS

Application of our method to isotopes of other elements will proceed similarly to the experiment described in this manuscript. Various laser wavelengths will be necessary for optical pumping of different elements. The operating temperature of the source will also vary for other elements, with many elements requiring source temperatures around 1000 ºC. Inductive heating should enable operation of sources to beyond 2500 ºC for certain high temperature elements such as molybdenum [30].

Mass independence

The magnetic guide will remain almost identical for many other elements. The exact arrangement of the guide will vary depending on the targeted isotope, as described in earlier work [10]. The reflective magnetic wall can easily be seen to be mass independent when considered in terms of energy: the wall presents a conservative potential barrier to an atom of

height μB, where μ is the atom's magnetic moment and B is the magnitude of the magnetic field in proximity to the wall. As long as this height is larger than the atom's kinetic energy determined by its velocity component perpendicular to the wall, the atom will not have enough energy to reach the magnets and will be reflected. As the transverse kinetic energy of an atom is determined by the source temperature T, a figure-of-merit for the guiding efficiency is μB/kT (with k denoting Boltzmann's constant), which is mass independent. To illustrate this point, μB/kT for mercury, one of the heaviest elements with mass 196, is seven times higher than for lithium due to its large magnetic moment and low operating temperature. As a result, the guide described in this work should in principle be much more efficient for mercury, reflecting the entire velocity profile.

Optical pumping of other elements

The concept of optical pumping was first proposed by Alfred Kastler in a landmark paper from 1950 [14], as he described in his 1966 Nobel Lecture. In that paper, Kastler showed that using polarized light and selection rules in atoms, it is possible to concentrate all the population in a particular magnetic state. He coined the term "lumino-refrigeration" to indicate that optical pumping creates a non-equilibrium state that has lower entropy than the initial state that is thermally populated. Since that time, optical pumping has become a standard tool in atomic physics. The invention of the laser and the development of new laser technologies that span the spectrum from UV to near-IR enable very efficient optical pumping.

Supplementary Table 1 outlines wavelengths that can be used for optical pumping of 27 elements, including 129 stable isotopes, in the periodic table. Only 254 stable isotopes are known to exist in nature, and 26 elements in the periodic table have only a single known stable

DOI: 10.1038/NPHYS3013

isotope. Therefore, our method should be applicable to at least 56% of all isotopes of interest in nature. Most of the cases that require multiple wavelengths correspond to elements with zero magnetic moment in the ground state. The auxiliary wavelengths are typically used just for preparing atoms in a metastable state. The lifetimes of these metastable states are typically at least several seconds. Supplementary Table 1 is not exhaustive, and transitions might exist for other elements in the periodic table.

For most transitions in the table, isotope shifts can be readily found in literature. These shifts range from hundreds of MHz to several GHz (references in Supplementary Table 1). Many other relevant spectroscopic data is available in literature including saturation intensities which yield a measure of transition cross-sections. Known saturation intensities for these transitions range from below 1 mW to close to 100 mW (references in Supplementary Table 1). Most isotopes with even mass number have zero nuclear spin, and thus no hyperfine structure. For isotopes with nonzero nuclear spin, multiple frequencies may sometimes be necessary to address different hyperfine states. These frequencies, however, will most often be derivable from a single laser with frequency shifters. The effect of nuclear spin on the efficiency of optical pumping will be isotope-dependent. Worst case scenarios might require several times the number of photons per atom as in the case of zero nuclear spin.

Certain transitions given in Supplementary Table 1 were used for laser cooling of a given element. In contrast to optical pumping, laser cooling requires many ($\sim 10^5$) cycles of a given transition per atom. To achieve this many cycles, these cycling transitions typically require that $\Delta J = +1$ between the excited and ground states. The cycling therefore not only necessitates high laser powers, but also often leads to the use of multiple lasers to ensure that atoms reliably return to the ground state of this cycling transition. For example, the most practical line for laser

cooling of iron (372 nm) decays to a metastable state that is no longer resonant with this transition after several hundred spontaneous emission events on average. Without using multiple lasers to circumvent this leakage, laser cooling is curtailed. In contrast, optical pumping on this transition should be possible, although the efficiency for transferring to the desired state will be limited by the fact that the transition is truly cycling with $\Delta J = +1$. A nearby transition at 368 nm with $\Delta J = 0$ might be better suited for our method. Other transitions listed in the table, like those for Mo, Ni, Gd, and Nd, will likely not enable laser cooling, but are sufficient for optical pumping.

Commercial solid-state laser systems are available that will provide at least 100 mW for almost all of the transition wavelengths in Supplementary Table 1. This power is generally sufficient to separate approximately 5 moles per year of a desired isotope. This quantity is relevant for most isotopes needed for nuclear medicine. Most commercial systems consist of readily available laser diodes and amplifiers. An alternative option to this combination, particularly further in the UV, is an optically pumped semiconductor laser (OPSL). OPSLs achieve very high powers (>1 W) by optically pumping a solid-state gain region, typically using a high power pump at around 800 nm. Controlling the fabrication of the gain region, emission wavelengths can be tailored to be between 900 – 1200 nm [31,32]. Using a frequency doubling cavity (commercially available), over 500 mW between 450 – 600 nm can be produced. With a second stage of frequency doubling over 200 mW between 225 – 300 nm can be achieved [33,34].

DOI: 10.1038/NPHYS3013

	Element	Stable Isotopes	Target State	λ(nm)	Refs.
1	Li	6,7	$2s\ ^2S_{1/2}$	670	23,35
2	Mg	24,25,26	$3s3p\ ^3P_2$ (2050 s)	457,383,384	36-39
3	Ar	36,38,40	$3s^23p^5(^2P_{3/2})4s\ ^3P_2$ (60 s)	811	40,41
4	K	39,40,41	$4s\ ^2S_{1/2}$	770	35,42
5	Ca	40,42,43,44,46,48	$4s4p\ ^3P_2$ (7000 s)	657,443,445	36-38,43,44
6	Cr	50,52,53,54	$3d^5(^6S)4s\ a^7S_3$	425	45,46
7	Fe	54,56,57,58	$3d^64s^2\ a^5D_4$	372	47,48
8	Ni	58,60,61,62,64	$3d^8(^3F)4s^2\ ^3F_4$	323	49
9	Cu	63,65	$3d^{10}4s\ ^2S_{1/2}$	327	50
10	Zn	64,66,67,68,70	$3d^{10}4s4p\ ^3P_2$ (>100 s)	308,330,335	51
11	Ga	69,70	$4s^24p\ ^2P_{3/2}$ (--)	403,294	52-54
12	Kr	78,80,82,83,84,86	$4s^24p^5(^2P_{3/2})5s\ ^3P_2$ (85 s)	811	40,55
13	Rb	85,87	$5s\ ^2S_{1/2}$	795	35,56
14	Sr	84,86,87,88	$5s5p\ ^3P_2$ (1000 s)	689,679,688,707	36-38,44,57,58
15	Mo	92,94,95,96,97,98,100	$4d^5(^6S)5s\ a^7S_3$	380,715	59-61
16	Ag	107,109	$4d^{10}(^1S)5s\ ^2S_{1/2}$	328	62
17	Cd	106,108,110,111,112,113, 114,116	$5s5p\ ^3P_2$ (>10 s)	326,346,361	63
18	In	113,115	$5p\ ^2P_{3/2}$ (--)	410,451	64,65
19	Xe	124,126,128,129,130,131, 132,134,136	$5p^5(^2P_{3/2})6s\ ^3P_2$ (150 s)	881	40,66
20	Ba	130,132,134,135,136,137, 138	$6s5d\ ^3D_2$ (60 s)	326,347,361	16,67
21	Nd	142,143,144,145,146,148, 150	$4f^46s^2\ ^5I_4$	472	68-70
22	Gd	152,154,155,156,157,158, 160	$4f^7(^8S)5d6s^2\ ^9D_6$	423	71
23	Dy	156,158,160,161,162,163, 164	$4f^{10}6s^2\ ^5I_8$	421	72-75
24	Er	162,164,166,167,168,170	$4f^{12}6s^2\ ^3H_6$	401	75-77
25	Yb	168,170,171,172,173,174, 176	$4f^{14}(^1S)6s6p\ ^3P_2$ (12 s)	556,458,494	36,78,79
26	Hg	196,198,199,200,201,202, 204	$5d^{10}(^1S)6s6p\ ^3P_2$ (7 s)	254,404,436,365	80,81
27	Tl	203,205	$6s^26p\ ^2P_{3/2}$ (0.15 s)	378,352	82,83

Supplementary Table 1: Optical pumping details for 27 elements, corresponding to 129 isotopes. Target states correspond to the ground states of the chosen optical pumping transitions. In cases where this is not the ground state of the atom, the state lifetime is given in parentheses. References point to relevant spectroscopic data including isotope shifts, hyperfine splittings, and cross-sections. Note that excitation to metastable states for noble gases requires a discharge.

Additional References (primarily supporting Supplementary Table 1)

27. Schünemann, U., Engler, H., Grimm, R., Weidemüller, M. & Zielonkowski, M. Simple scheme for tunable frequency offset locking of two lasers. *Review of Scientific Instruments* **70**, 242-243 (1999).

28. Anderson, B. P. & Kasevich, M. A. Loading a vapor-cell magneto-optic trap using light-induced atom desorption. *Physical Review A* **63**, 023404 (2001).

29. Mecea, V. M. Is quartz crystal microbalance really a mass sensor? *Sensors and Actuators A: Physical* **128**, 270-277 (2006).

30. Ross, K. J. & Sonntag, B. High temperature metal atom beam sources. *Review of Scientific Instruments* **66**, 4409-4433 (1995).

31. Chilla, J. L. a. *et al*. High-power optically pumped semiconductor lasers. *Proc*. *Soc*. *Photo-Opt*. *Instrum*. *Eng*. **5332**, 143-150 (2004).

32. Ostroumov, V. *et al*. 1 W 488 nm cw air-cooled optically pumped semiconductor laser. *Proc*. *Soc*. *Photo-Opt*. *Instrum*. *Eng*. **6871**, 687118–1 (2008).

33. Kaneda, Y. *et al*. Continuous-wave all-solid-state 244 nm deep-ultraviolet laser source by fourth-harmonic generation of an optically pumped semiconductor laser using $CsLiB_6O_{10}$ in an external resonator. *Optics Letters* **33**, 1705-1707 (2008).

34. Paul, J. *et al*. Doppler-free spectroscopy of mercury at 253.7 nm using a high-power, frequency-quadrupled, optically pumped external-cavity semiconductor laser. *Optics Letters* **36**, 61-63 (2010).

35. Arimondo, E., Inguscio, M. & Violino, P. Experimental determinations of the hyperfine structure in the alkali atoms. *Reviews of Modern Physics* **49**, 31-75 (1977).

36. Loftus, T., Bochinski, J. R. & Mossberg, T. W. Magnetic trapping of ytterbium and the alkaline-earth metals. *Physical Review A* **66**, 013411 (2002).

37. Derevianko, A. Feasibility of Cooling and Trapping Metastable Alkaline-Earth Atoms. *Physical Review Letters* **87**, 023002 (2001).

38. Celikov, A. A., Akulshin, A. M., Velichansky, V. L. & Zibrov, A. S. Doppler-Free Spectroscopy of the 5^1S_0–5^3P_1 Strontium Intercombination Transition. *Laser Physics* **5**, 739-746 (1995).

39. Sterr, U., Sengstock, K., Müller, J. H. & Ertmer, W. High-Resolution Isotope Shift Measurement of the Mg I $^1S_0$ - $^3P_1$ Intercombination Transition. *Applied Physics B: Photophysics and Laser Chemistry* **56**, 62-64 (1993).

40. Metcalf, H. J. & Van der Straten, P. *Laser Cooling and Trapping*. (Springer, New York: 1999).

41. Williams, W. *et al*. Spectroscopic study of the cycling transition $4s[3/2]_2$–$4p[5/2]_3$ at 811.8 nm in ^{39}Ar: Hyperfine structure and isotope shift. *Physical Review A* **83**, 012512 (2011).

DOI: 10.1038/NPHYS3013

42. Williamson III, R. S. *Magneto-optical trapping of potassium isotopes*, Ph.D. Thesis, University of Wisconsin - Madison (1997).

43. Mollema, A. K. *Laser cooling, trapping and spectroscopy of calcium isotopes*, Ph.D. Thesis, University of Groningen (2008).

44. Lorenzen, C. -J., Niemax, K. & Pendrill, L. R. Isotope shifts of energy levels in the naturally abundant isotopes of strontium and calcium. *Physical Review A* **28**, 2051-2058 (1983).

45. Schmidt, P. O. *Scattering properties of ultra-cold chromium atoms*, Ph.D. Thesis, University of Stuttgart (2003).

46. Furmann, B., Jarosz, A., Stefańska, D., Dembczyński, J. & Stachowska, E. Isotope shift in chromium. *Spectrochimica Acta Part B: Atomic Spectroscopy* **60**, 33-40 (2005).

47. Krins, S., Oppel, S., Huet, N., von Zanthier, J. & Bastin, T. Isotope shifts and hyperfine structure of the Fe I 372-nm resonance line. *Physical Review A* **80**, 062508 (2009).

48. Smeets, B. *et al*. Laser collimation of an Fe atomic beam on a leaky transition. *Applied Physics B: Lasers and Optics* **80**, 833-839 (2005).

49. Steudel, A., Triebe, U. & Wendlandt, D. Isotope Shift in Ni I and Changes in Mean-Square Nuclear Charge Radii of the Stable Ni Isotopes. *Zeitschrift für Physik A -- Atoms and Nuclei* **296**, 189-193 (1980).

50. Kim, J. J. & Sung, N. Stimulated emission in optically pumped atomic-copper vapor. *Optics Letters* **12**, 885-887 (1987).

51. Hately, G. F. & Littlefield, T. A. Isotope Shift in the Arc Spectrum of Zinc. *Journal of the Optical Society of America* **48**, 851-853 (1958).

52. Maragò, O. M., Fazio, B., Gucciardi, P. G. & Arimondo, E. Atomic gallium laser spectroscopy with violet/blue diode lasers. *Applied Physics B: Lasers and Optics* **77**, 809-815 (2003).

53. Rehse, S. J., Bockel, K. M. & Lee, S. A. Laser collimation of an atomic gallium beam. *Physical Review A* **69**, 063404 (2004).

54. Rehse, S. J., Fairbank, Jr., W. M. & Lee, S. A. Measurement of the hyperfine structure of the $4d^2D_{3/2,5/2}$ levels and isotope shifts of the $4p^2P_{3/2} \rightarrow 4d^2D_{3/2}$ and $4p^2P_{3/2} \rightarrow 4d^2D_{5/2}$ transitions in gallium 69 and 71. *Journal of the Optical Society of America B* **18**, 855-860 (2001).

55. Chen, C. Y, *et. al*. Ultrasensitive Isotope Trace Analyses with a Magneto-Optical Trap. *Science* **286**, 1139-1141 (1999).

56. Barwood, G. P., Gill, P. & Rowley, W. R. C. Frequency Measurements on Optically Narrowed Rb-Stabilised Laser Diodes at 780 nm and 795 nm. *Applied Physics B: Photophysics and Laser Chemistry* **53**, 142-147 (1991).

57. Xu, X., Loftus, T. H., Hall, J. L., Gallagher, A. & Ye, J. Cooling and trapping of atomic strontium. *Journal of the Optical Society of America B* **20**, 968-976 (2003).

58. Hughes, R. H. Isotope Shifts in the Spectra of Strontium. *Physical Review* **105**, 1260-1261 (1957).

59. Hancox, C. I., Hummon, M. T., Nguyen, S. V. & Doyle, J. M. Evaporative cooling of magnetically trapped atomic molybdenum. *Physical Review A* **71**, 031402 (2005).

60. Aufmuth, P. *et al*. Isotope Shift in Molybdenum. *Zeitschrift für Physik A -- Atoms and Nuclei* **285**, 357-364 (1978).

61. Whaling, W. & Brault, J. W. Comprehensive transition probabilities in Mo I. *Physica Scripta* **38**, 707-718 (1988).

62. Uhlenberg, G., Dirscherl, J. & Walther, H. Magneto-optical trapping of silver atoms. *Physical Review A* **62**, 063404 (2000).

63. Kloch, R. *et al*. Isotope shifts in λ326.1 nm of CdI. *Zeitschrift für Physik D -- Atoms, Molecules and Clusters* **6**, 315-317 (1987).

64. Klöter, B., Weber, C., Haubrich, D., Meschede, D. & Metcalf, H. Laser cooling of an indium atomic beam enabled by magnetic fields. *Physical Review A* **77**, 033402 (2008).

65. Lorenzen, C.-J., Niemax, K. & Weber, K.-H. Level isotope shifts of indium 113 and 115. *Optics Communications* **52**, 178-182 (1984).

66. Walhout, M., Megens, H. J. L., Witte, A. & Rolston, S. L. Magneto-optical trapping of metastable xenon: Isotope-shift measurements. *Physical Review A* **48**, R879-R882 (1993).

67. De, S. *Laser cooling and trapping of barium*, Ph.D. Thesis, University of Groningen (2008).

68. Gorshkov, V. N., Komarovskii, V. A., Osherovich, A. L. & Penkin, N. P. Lifetimes of excited levels of Nd I and Nd II. Oscillator strengths of the spectral lines of Nd I. *Astrophysics* **17**, 437-441 (1982).

69. Den Hartog, E. A., Fittante, A. J. & Lawler, J. E. Radiative lifetimes of neutral neodymium. *Journal of Physics B: Atomic, Molecular and Optical Physics* **44**, 225001 (2011).

70. Stockett, M. H., Wood, M. P., Den Hartog, E. A. & Lawler, J. E. Atomic transition probabilities of Nd I. *Journal of Physics B: Atomic, Molecular and Optical Physics* **44**, 235003 (2011).

71. Blaum, K., *et al*. Isotope shifts and hyperfine structure in the $[Xe]4f^7 5d6s^2\ ^9D_J \rightarrow [Xe]4f^7 5d6s6p\ ^9F_{J+1}$ transitions of gadolinium. *The European Physical Journal D* **11**, 37-44 (2000).

72. Leefer, N. *et al*. Transverse laser cooling of a thermal atomic beam of dysprosium. *Physical Review A* **81**, 043427 (2010).

73. Leefer, N., Cingöz, A. & Budker, D. Measurement of hyperfine structure and isotope shifts in the Dy 421 nm transition. *Optics Letters* **34**, 2548-2550 (2009).

DOI: 10.1038/NPHYS3013

74. Lu, M., Youn, S. H. & Lev, B. L. Spectroscopy of a narrow-line laser-cooling transition in atomic dysprosium. *Physical Review A* **83**, 012510 (2011).

75. Jin, W.-G., Ono, H. & Minowa, T. Isotope Shifts in High Lying Levels of Dy I and Er I by High-Resolution UV Laser Spectroscopy. *International Journal of Spectroscopy* **2011**, 1-5 (2011).

76. McClelland, J. J. & Hanssen, J. L. Laser Cooling without Repumping: A Magneto-Optical Trap for Erbium Atoms. *Physical Review Letters* **96**, 143005 (2006).

77. Ban, H. Y., Jacka, M., Hanssen, J. L., Reader, J. & McClelland, J. J. Laser cooling transitions in atomic erbium. *Optics Express* **13**, 3185-3195 (2005).

78. Maruyama, R. *Optical Trapping of Ytterbium Atoms*, Ph.D. Thesis, University of Washington (2003).

79. Pandey, K., Singh, A. R., Kumar, P. V. K., Suryanarayana, M. V. & Natarajan, V. Isotope shifts and hyperfine structure in the 555.8-nm $^1S_0 \rightarrow {}^3P_1$ line of Yb. *Physical Review A* **80**, 022518 (2009).

80. Villwock, P., Siol, S. & Walther, T. Magneto-optical trapping of neutral mercury. *The European Physical Journal D* **65**, 251 (2011).

81. Schweitzer, Jr., W. G. Hyperfine Structure and Isotope Shifts in the 2537-Å Line of Mercury. *Journal of the Optical Society of America* **51**, 692-693 (1961).

82. Schuler, C. J., Çiftan, M., Bradley, III, L. C. & Stroke, H. H. Hyperfine Structure and Isotope Shift in the $7^2S_{½}$ - $6^2P_{½}$ Transition of Natural Thallium by Atomic Beam Absorption. *Journal of the Optical Society of America* **52**, 501-503 (1962).

83. Fan, I. *et al*. Prospects of laser cooling in atomic thallium. *Physical Review A* **84**, 042504 (2011).